International Forum on Aeroelasticity and Structural Dynamics
IFASD 2017
25-28 June 2017 Como, Italy

CFD MODEL OF THE TRANSONIC DYNAMICS TUNNEL WITH APPLICATIONS

Pawel Chwalowski, Walter A. Silva, Carol D. Wieseman and Jennifer Heeg[1]

[1]Aeroelasticity Branch, NASA Langley Research Center, Hampton, VA 23681, USA
Pawel.Chwalowski@nasa.gov

Keywords: Computational Aeroelasticity, Dynamic Aeroelastic, Flutter, FUN3D.

Abstract: This paper presents the Computational Fluid Dynamics (CFD) model of the flow in the NASA Langley Research Center Transonic Dynamics Tunnel (TDT) with some recent applications. The TDT is a continuous-flow, closed circuit, slotted-test-section wind tunnel with a 16- by 16-foot test section with cropped corners. The tunnel was originally built as the 19-ft Pressure Tunnel in 1938, but it was converted to the current transonic tunnel in the 1950s, with capabilities to use either air or heavy gas at pressures from atmosphere down to near vacuum. In this study, experimental data acquired in the empty tunnel using R-134a as the test medium was used to calibrate the computational data. Experimental data from a recent TDT test of a full-span fighter configuration in air was then selected for comparison with the numerical data. During this test, the configuration experienced a flutter event in the transonic flow regime. Numerically, the flutter event is simulated both inside the CFD model of the TDT and in a classical free-air model. The preliminary results show that the wind-tunnel walls do affect the response of the tested vehicle but do not affect overall flutter prediction.

1 INTRODUCTION

In a typical wind-tunnel experiment of a wall-mounted or sting-mounted model, the tested structure is mounted away from the tunnel walls to avoid wall interference effects. The wall interference includes boundary-layer development upstream of the tested structure along the tunnel walls. The distance required to mount the structure away from the tunnel walls is usually well known and carefully incorporated into the test hardware. However, during the test of the Rectangular Supercritical Wing [1–3] in the NASA Langley Transonic Dynamics Tunnel (TDT), the wing was mounted on a splitter plate located only half the desired distance from the wall. For the first Aeroelastic Prediction Workshop [4–6] held in April 2012, the workshop participants attempted to calculate pressure distribution on that wing. Several combinations of the computational models were generated to account for the boundary-layer development ahead of the wing, but the calculated surface pressure did not match the experimental data well. Consequently, the idea to create a computational model of the TDT to account for tunnel-wall effects was conceived and initiated in 2012. This paper outlines the steps to generate and test the Computational Fluid Dynamics (CFD) model of the TDT.

It is important to emphasize that before any test article is modeled within a CFD version of the TDT for computational testing and analysis, the fundamental tunnel calibration quantities obtained in an empty tunnel in any test medium, air or heavy gas, have to be matched between the experiment and computations. For the TDT, these experimental quantities were obtained

during tunnel calibration experiments conducted in the mid to late 1990s and include wall pressure measurements near the centerline for each of the four walls along the entire test section leg of the tunnel, boundary-layer measurements at six locations, and the centerline Mach number measurements spanning the entire distance of the test section leg of the tunnel.

The TDT, located at the NASA Langley Research Center, is a continuous-flow, closed circuit, slotted-test-section wind tunnel, with a 16- by 16-foot test section with cropped corners. The tunnel was originally built in 1938, but was converted to the current transonic tunnel in the 1950s, with capabilities to use either air or R-134a heavy gas as the test medium. In this study, experimental data acquired in the empty tunnel using the R-134a test medium was used to calibrate the computational data. TDT's unique capabilities are well described and summarized in the recent publication by Ivanco [7], where he states the following: "Typically regarded as the world's premier aeroelastic test facility, TDT fulfills a unique niche in the wind tunnel infrastructure as a result of its unparalleled ability to manipulate fluid-structure scaling parameters."

Much has been published on the topic of wind-tunnel wall interference. Most notably, publications by Krynytzky [8–10] defined wall interference issues associated with large transonic wind tunnels, including the TDT and the Boeing Transonic Wind Tunnel. He also used CFD analyses [9, 10] to calibrate numerical models against experimental data, which included boundary-layer profiles and test section centerline Mach number distribution. In 2004, Glazkov [11] made an assessment of the slot flow and wall interference for the European Transonic Windtunnel. More recently, Olander [12] and Neumann [13] incorporated wind-tunnel walls in CFD models and obtained good comparisons between the computational and experimental data. On the other hand, Massey [14] incorporated TDT wind-tunnel walls in his rotorcraft research and did not see any influence of the walls on CFD results.

The purpose of this paper is not to offer a replacement of the experimental data with the computational analysis. It is to show that in some flow regimes, computational methods are mature enough to complement wind-tunnel testing, while in other flow regimes, modeling the wind-tunnel flow environment is more difficult and requires further refinement of simulation parameters. The fundamental technical challenges include the size of the computational domain, the details of the tunnel geometry, and the specification of the boundary conditions. The following statement by Krynytzky [10] accurately describe challenges in computational modeling of the TDT: "Modeling simplifications and choices are still necessary and opportunities for both glory and humiliation abound."

In 1985 and 1986, two wind-tunnel models of the Saab JAS 39 Gripen were designed, built, and tested in the TDT for flutter clearance. One model, referred to as the stability model, was designed to be stiff but incorporated proper scaling of both the mass and geometry. The other model, referred to as the flutter model, was designed for proper scaling of structural dynamics properties and was used for flutter testing with various external stores attached. Currently, the Royal Institute of Technology (KTH) in Sweden and the NASA Langley Research Center are collaborating in testing a single generic fighter flutter-model based on these earlier models [15–17]. The new model has a similar outer mold line (OML) to the Gripen, but it has been modified to provide a more generic fighter configuration. The model was tested in the summer of 2016. Large amounts of data were acquired, including steady/unsteady pressures, accelerations, and measured dynamic deformations. During testing, a flutter event occurred, which damaged the wings. This flutter event has been predicted in computational models with and without tunnel walls and the results are presented herein.

2 EMPTY TUNNEL COMPUTATIONAL MODEL

2.1 Computational Geometry

The plan view of the TDT is shown in Figure 1a. Details of the slot locations in the test section leg are identified in Figure 1b. Note that in this drawing the 'TS' stands for tunnel station in dimensions of feet. The entrance to the test section is at TS 26, and the ceiling and floor slots begin at TS 50 and end at TS 80. The side-wall slots begin at TS 64 and end at TS 80. Tunnel station 72 coincides with the center of the east wall turntable where wall-mounted models are installed. The red line in Figure 1a around the test section of the tunnel shows the outline of the computational domain used in the CFD analysis. The domain begins with the settling chamber and continues into the test section leg, where it is connected with the plenum via slots in all four walls and a system of re-entry flaps. The domain ends with the diffuser. The shape of the computational domain at the settling chamber is not desirable for the numerical analysis because of the corners where the east and west walls of the chamber meet the turning vanes. However, to include the turning vanes in the computational model together with the rest of the tunnel geometry is too computationally expensive at this time.

The TDT uses a scheduled system of re-entry flaps in the floor and ceiling just downstream of TS 80 to recapture the working fluid that expands into the plenum. There are four predefined flap positions, each associated with a particular Mach number range. Figure 2 presents details about the flaps, with the layout shown in Figure 2a and the four operational positions identified in Figure 2b.

This study utilizes an 'as-built' surface geometry of the TDT as opposed to 'per-drawing'. The same approach was used by Nayani [18] in his analysis of the NASA Langley 14- by 22-ft low-speed wind tunnel. To obtain 'as-built' geometry for both tunnels, a laser scan of the desired regions was conducted. The laser scan produced a point cloud database of approximately 15.5 million points through which surfaces were fitted in preparation for grid generation. The details of the surface-fitting process can be found in reference [19].

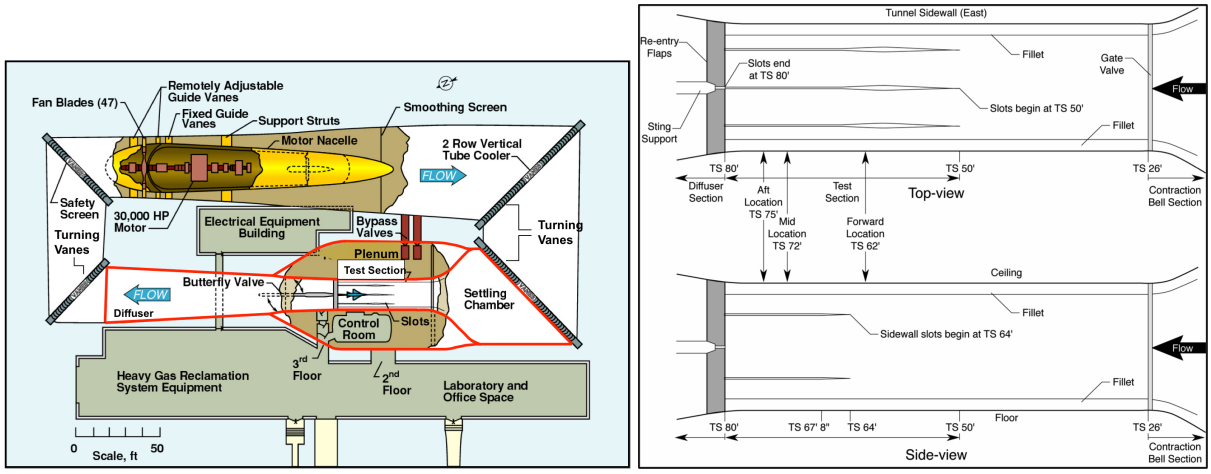

(a) TDT plan view with computational domain marked in red.

(b) Schematic of TDT showing the location of the slots.

Figure 1: TDT description.

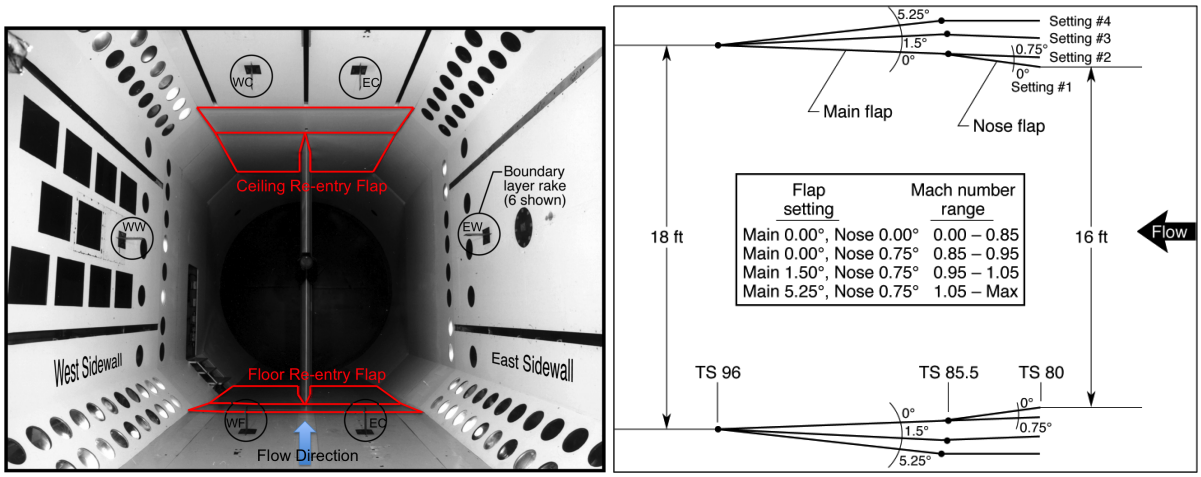

(a) TDT test section with boundary-layer rakes and re-entry flaps outlined.

(b) Re-entry flaps schedule as a function of Mach number.

Figure 2: Boundary-layer rakes mounted inside the TDT and the layout with operational schedule for the re-entry flaps.

2.2 Computational Mesh

Unstructured tetrahedral grids were used in this study. They were generated using VGRID [20] with input prepared using GridTool [21]. The tetrahedral elements within the boundary layer were converted into prism elements using preprocessing options within the NASA Langley FUN3D software [22]. First-cell height away from the wall was set to 9×10^{-6} feet, which ensured the average $y^+ < 1$. The typical mesh size was about 72 million nodes, or approximately 400 million elements.

Figure 3 shows examples of the mesh used throughout the computational domain. The particular mesh shown corresponds to the fourth re-entry flap setting, used in the computations of the supersonic flow (Mach 1.1) condition in the test section. Each flap setting identified in Figure 2b required a separate mesh (not shown here). For example, the analysis of the subsonic flow in the test section required a construction of the mesh with the re-entry flap closed.

2.3 Flow Solver and Solution Process

FUN3D software, which was developed at the NASA Langley Research Center, was used in this analysis. FUN3D is a finite-volume, unstructured-grid, node-based, mixed-element RANS flow solver. Various turbulence models are available, but in this study, the turbulence closure was obtained using the Spalart-Allmaras one-equation model. Flux limitation was accomplished with the minmod limiter [23]. Inviscid fluxes were computed using the Roe flux-difference splitting scheme [24]. For the asymptotically-steady cases under consideration, time integration was accomplished by an Euler implicit backwards difference scheme, with local time stepping to accelerate convergence. Most of the steady-state cases in this study were run for about 8000 iterations to achieve an approximate seven order-of-magnitude drop in residuals.

A total pressure and total temperature boundary condition was used at the inlet. For simplicity in this initial study, the inlet flow angle was assumed to be normal to the inlet plane, even though this flow angle is not accurate since the working fluid enters the test section leg at the angle closer to the turning-vane angle. Future analyses will quantify the effects of flow angle on the computed pressures. At the exit to the computational domain, a back pressure

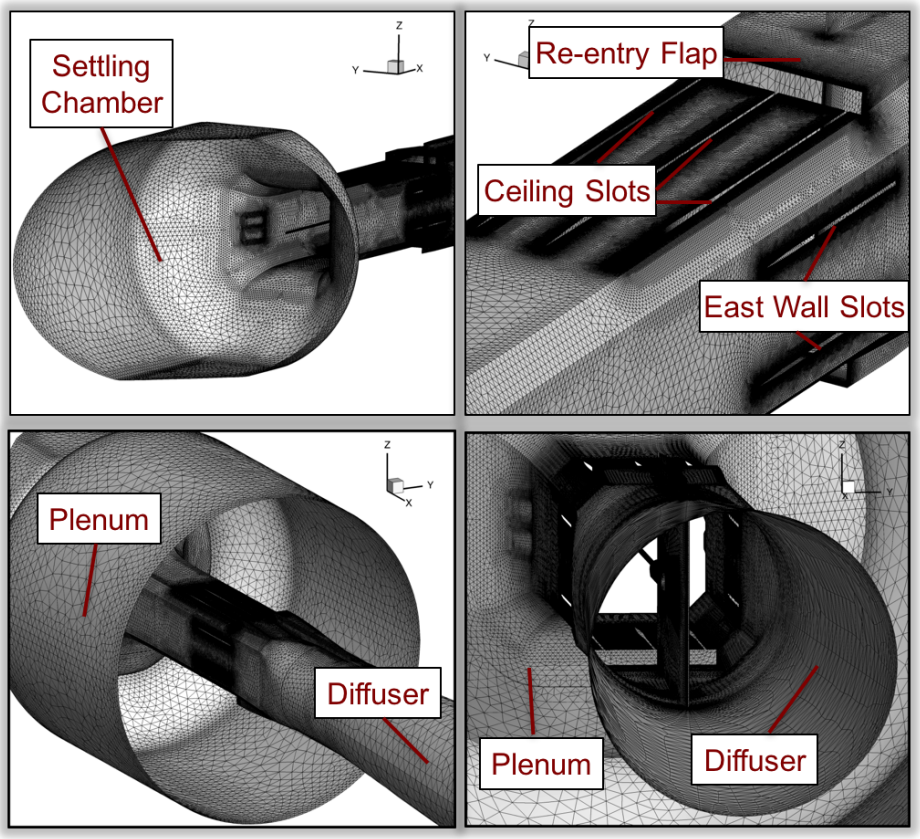

Figure 3: Computational mesh examples with a re-entry flap configuration corresponding to the Mach > 1.05 setting.

boundary condition was used. The value of this back pressure was iterated to achieve the desired Mach number in the test section. Every computation was run 'from scratch' when the back pressure was changed, even for the subsonic flow cases. This procedure was adopted after it was observed that restarting a solution from the previous solution with the change in back pressure resulted in oscillations in the flow field requiring many iterations to damp out.

In a typical solution, the flow was initialized to total pressure and total temperature in the settling chamber and to the static pressure elsewhere. This method produced the solution in the fewest iterations. However, due to the geometric complexity of the computational domain, two other methods of flow initialization were tested. In one method, the entire computational domain was initialized to the total pressure and total temperature and in the other method the computational domain was initialized to just the static pressure. Each steady-state computation took approximately 12 hours on 768 Sandy Bridges cores on the Pleiades computer at the NASA Advanced Supercomputing (NAS) Division.

The empty-tunnel wall pressure, boundary layer, and centerline Mach number experimental data, consisted of static pressure measurements. The static pressures were then converted into Mach numbers using isentropic flow relations. A similar process was adopted in the computational results. Most of the results in this study, with the exception of boundary-layer data, are presented as Mach numbers computed from the pressure along the length of the test section leg of the tunnel. The boundary-layer data is presented as a velocity ratio of local velocity to freestream velocity plotted versus perpendicular distance to the tunnel walls.

3 EMPTY TUNNEL CALIBRATION DATA

The empty-tunnel experimental data used to calibrate the CFD model of the flow in the TDT with the R-134a as the test medium consisted of three sets: boundary-layer profiles, wall pressures, and centerline Mach number data. The tunnel conditions used are summarized in Table 1. Only selected results, mainly at Mach 1.1, are presented here. Additional computational results were published previously [19].

Table 1: Computational Parameters.

Mach number	q, psf	P_t, psf	T_t, °F	Re/ft, x 10^{-6}	Re-entry Flap Setting
0.5	87.6	635.4	90.8	2.487	#1
0.7	157.9	761.7	97.4	3.204	#1
1.1	307.7	880.5	130.1	3.923	#4

3.1 Boundary-Layer Calibration

The experimental boundary-layer measurements in the TDT were acquired in 1998 and are documented by Wieseman and Bennett [25]. A group of six boundary-layer rakes were mounted at one of three stations (TS 62, 72, 75) to measure the boundary layer in the empty tunnel: two on the floor, two on the ceiling, one on the east wall and one on the west wall. The locations of the rakes at one tunnel station, together with their labels, are shown in Figure 2a. The labels of the rakes are as follows: EW means 'east wall', EC means 'east ceiling', EF means 'east floor', WW means 'west wall', WC means 'west ceiling', and WF means 'west floor'. The pressure tubes from the rakes were connected to electronically-scanned pressure modules. Boundary-layer profiles were determined from the measured pressures and the associated tunnel conditions.

For this study, the focus was on the boundary-layer profiles at TS 72. The numerical boundary layer was computed by extracting a plane at tunnel station 72 from the solution. A Tecplot^{TM} [26] macro was then used to extract velocity at each rake location. The results at Mach 1.1 are presented in Figure 4 as a velocity ratio plotted in the direction perpendicular to the mounting wall for each rake. The experimental data in these figures includes minimum (min), maximum (max), and statistical mean (mean) values of the velocities. The agreement between the experimental and computational data is good considering the flow-angle assumption at the inlet of the computational domain. The most notable differences are observed at the east wall. As previously discussed, the limitations in the computational domain choices upstream of the east wall may affect the computational results. However, in general, the experimental data also suggests one of two things. Either the experimental instrumentation used was not adequate for pressure measurements at below atmospheric pressure, or the boundary layer in the tunnel exhibits very dynamic behavior. These experimental results suggest the need to repeat the boundary-layer measurement experiment.

3.2 Wall Pressure Calibration

The wall pressure measurements in the TDT were also conducted in 1998 and were documented by Florance [27]. In this experiment, static pressure ports were installed in the test section walls flush with the surface. The floor static ports, labeled in green in Figure 5a, were located midway

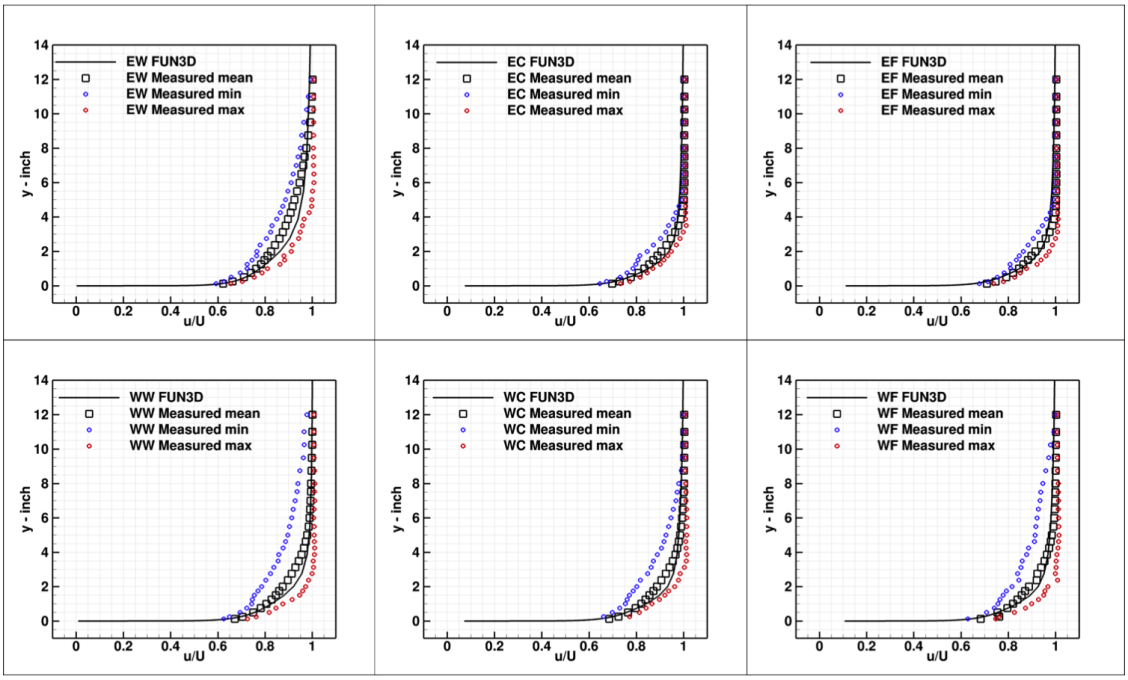

Figure 4: Experimental and computational boundary-layer profiles at Mach 1.1.

between the floor centerline slot and the east floor slot. The ceiling static ports, labeled in blue in Figure 5a, were located midway between the ceiling centerline slot and the west ceiling slot. The east and west wall ports were located approximately along the centerline of the east and west walls and are labeled in red and orange, respectively, in Figure 5a. Mach numbers from the measured sidewall static pressures and the associated tunnel conditions were computed using isentropic flow relations.

Because the exact locations of the pressure sensors were known, the static pressure values were extracted from the computational solutions at these locations. Mach numbers were subsequently computed from these pressure values. The comparisons between the experimentally- and computationally-obtained Mach numbers are shown in Figure 5. The agreement is very good, with the largest differences noticed around tunnel station 65 for the Mach 1.1 condition.

3.3 Centerline Mach Number Calibration

The centerline Mach number experiments were conducted in the TDT in 1999 by Keller [28]. In this experiment, a 60-foot long 6-inch diameter aluminum tube was installed in the center of the tunnel. The tube, shown in Figure 6, was mounted on the TDT sting/splitter-plate assembly and was also supported by several steel cables along its length. Static pressure sensors on the tube started at TS 40 and were spaced every six inches between tunnel stations 40 and 56 and every three inches between tunnel stations 58 and 80. As before, the measured static pressures, together with tunnel conditions, were converted into Mach numbers using isentropic flow equations. Computationally, a Tecplot cutting plane across the tube was used to extract corresponding static pressures. The computational results and the experimental data are compared in Figure 7a. There is excellent agreement at both Mach 0.5 and 0.7. However, some discrepancy is present at Mach 1.1, which required further analysis.

Figure 7b focuses on these additional Mach 1.1 results. The first consideration is the data between tunnel station 45 and 50, just ahead of the ceiling and floor slots. The experimental data

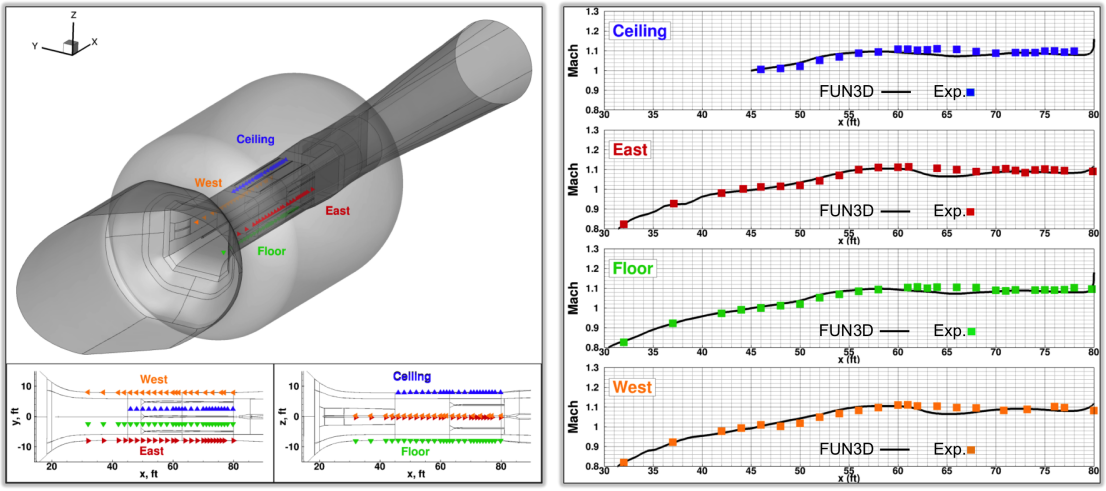

(a) Location of pressure sensors.

(b) Mach 1.1 results.

Figure 5: TDT wall pressure measurement locations with corresponding experimental and computational Mach number distributions (Mach 1.1).

shows a choked flow (Mach number equal 1), with a slight flow acceleration above Mach 1 at tunnel station 45. The computational results do not show choked flow; the flow slightly accelerates through that region, with a distinct flow acceleration near tunnel station 52. The light blue curve with black dashes in Figure 7b shows the cross-sectional area of the tunnel between stations 30 and 80. According to the laser scan and the surface fitting process described previously, the minimum cross sectional area in the test section leg of the tunnel is at tunnel station 44. A gradual increase in the cross sectional area is observed between tunnel stations 44 and 62, with a nearly constant area from there up to tunnel station 80. The physical area distribution as opposed to the aerodynamic area supports the computational results. The gradual flow acceleration follows the physical cross-sectional area of the tunnel. One possible explanation of the mismatch in computational and experimental data in this region is that the computational mesh is too coarse to capture the true aerodynamic area. Another possibility is that the laser scan and/or surface fitting through the cloud of points obtained from the laser scan is not correct. It was also suggested that the geometry of the tunnel itself undergoes small changes during the supersonic flow testing, affecting cross-sectional area. In addition, the effects of cables supporting the tube are not accounted for in the computational model. Finally, there is a possibility that the experimental centerline Mach number distribution is affected by the presence of the tube itself. It is difficult to verify this statement since the only source of the experimental data is from the centerline tube experiment. It is possible, however, to remove the tube in the numerical model and examine the centerline Mach number. The results are not shown here, but it appears that the presence of the tube does not affect the centerline Mach number distribution obtained numerically.

The red curve in Figure 7b was obtained with both the tunnel slots and the re-entry flaps open (flap setting #4). To verify the computational results at Mach 1.1, the solution with the same boundary conditions (i.e., total pressure and temperature and the static back pressure) was obtained using the mesh with flap setting #1. This means that the slots were left open, but the re-entry flaps were closed. With this check, it was anticipated that the flow would expand and re-enter the tunnel through the slots at the same time, resulting in a choked flow with Mach number near 1. The computational result, shown in purple in Figure 7b, confirmed this expectation. Corresponding experimental data for this theoretical condition is not available

since in the experiment, the re-entry flaps were always set to position #4 at Mach 1.1.

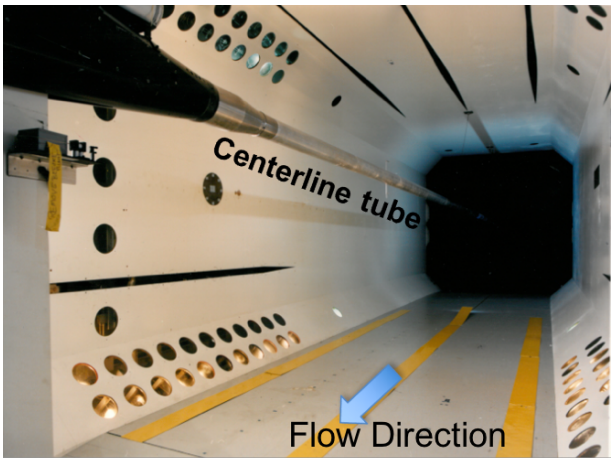

Figure 6: Centerline tube inside the TDT.

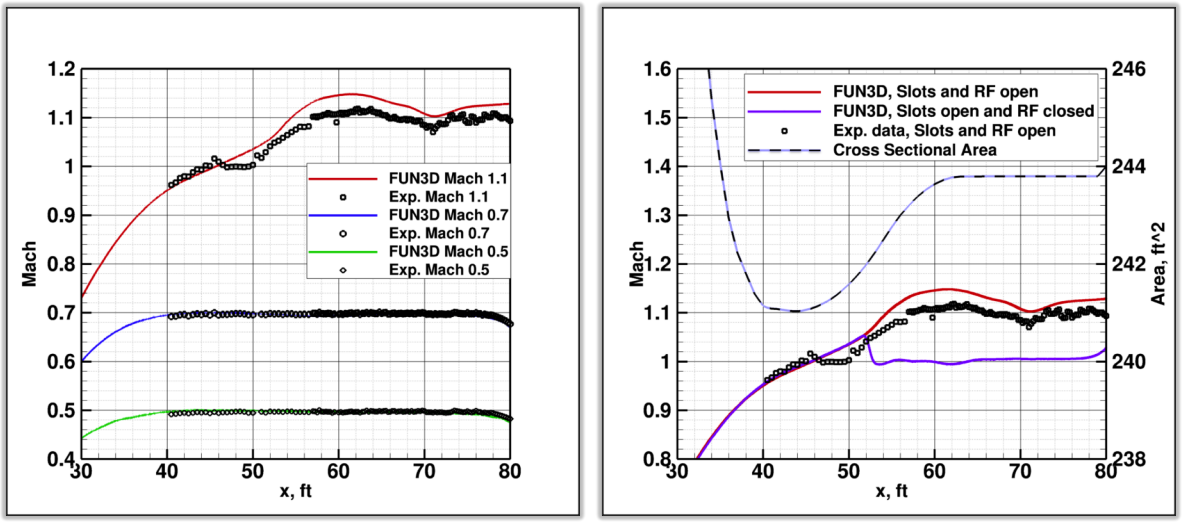

(a) Mach 0.5, 0.7, and 1.1 plotted together.

(b) Mach 1.1 with slots and re-entry flaps (RF) open; Mach 1.1 with slots open and re-entry flaps closed; and tunnel cross sectional area.

Figure 7: Computed and measured centerline Mach numbers at Mach 0.5, 0.7, and 1.1.

4 SLOT FLOW

Mach number contours at tunnel station 72 for the two out of three cases considered in this study are shown in Figure 8. This figure demonstrates that as Mach number in the test section increases the expansion of the fluid into the TDT plenum also increases. The same conclusion can be drawn based on the Mach contours shown in Figures 9 and 10. Figure 9 shows Mach number contours at the plane cutting through the ceiling and floor center slots for the Mach 0.5 case. Figure 10 shows Mach number contours at the plane cutting through the ceiling and floor center slots for the Mach 1.1 case.

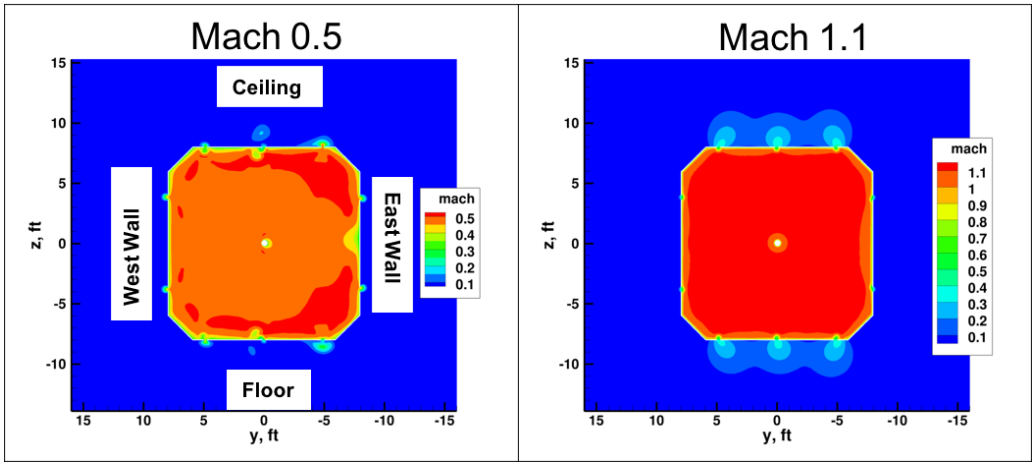

Figure 8: Mach number contours at tunnel station 72: Mach 0.5 and 1.1.

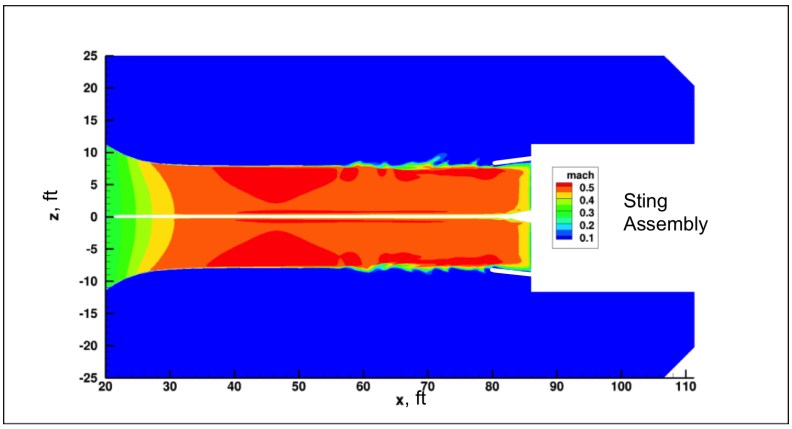

Figure 9: Mach number contours across the ceiling and floor center slots at Mach 0.5 case corresponding to the green curve in Figure 7a.

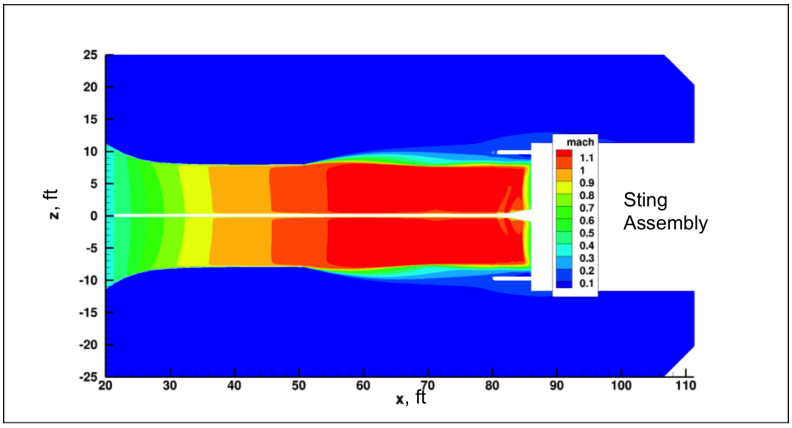

Figure 10: Mach number contours across the ceiling and floor center slots at Mach 1.1 case corresponding to the red curve in Figure 7b; re-entry flaps in position #4.

5 KTH WIND-TUNNEL COMPUTATIONAL MODEL

As stated earlier in the introduction, during 2016 testing of the KTH model in the TDT, a flutter event occurred near the Mach 0.9 flow condition, which damaged both wings. This flutter event has been predicted numerically using FUN3D software. The geometry of the full-span KTH fighter configuration was integrated into the CFD model of the TDT and analyzed. This configuration is referred to as a KTH-TDT model in this study. The results from this analysis were then compared with results where the computational domain did not include tunnel walls. This model is called a KTH-FA (free-air) model. The purpose of this comparison was to determine if the flutter boundary prediction in the transonic flow was affected by the presence of the tunnel walls. Because of the geometric simplifications imposed on the aerodynamic model and described below, the trends in flutter predictions between the KTH-TDT and the KTH-FA models are emphasized here as opposed to the direct comparison between the experimental and computational flutter data.

Figure 11a shows the KTH wind-tunnel model installed in the TDT. The model configuration in Figure 11a shows stores under the wing and tip missiles on rails at the wing tips. However, a "clean wing" configuration with just the wing tip missiles was also tested. The wind-tunnel flutter event occurred during testing of a modified, high-risk configuration with the stores and missiles where ballast was added at the wing tips.

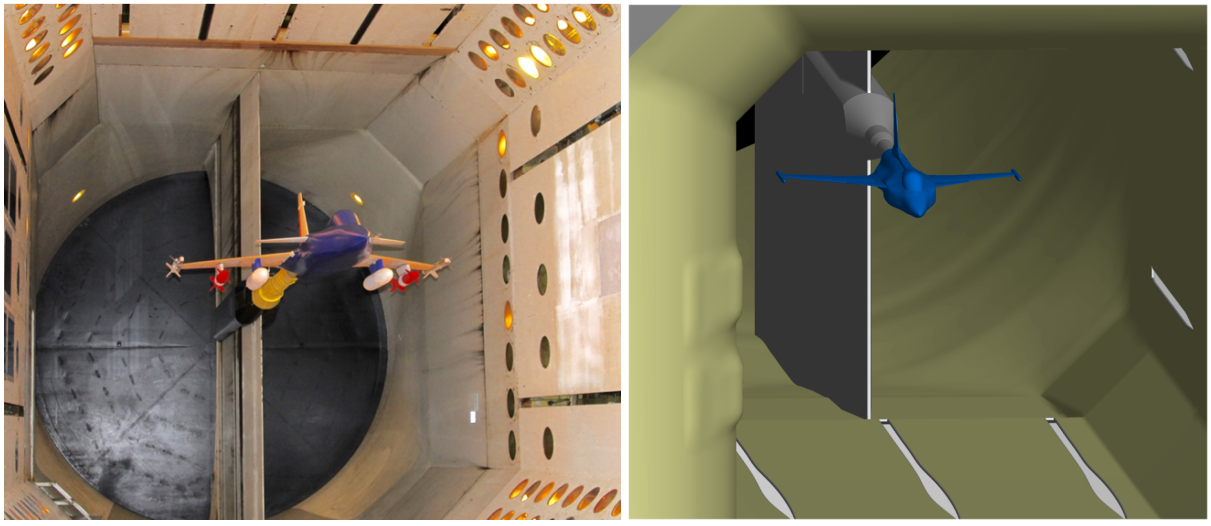

(a) Sting-mounted in the TDT. (b) As "installed" in the TDT CFD model

Figure 11: The KTH generic fighter aeroelastic model.

5.1 Computational Model

The computational domain in the KTH-FA model consisted of the outer boundary located about 100-chord lengths away from the aircraft geometry. The aircraft geometry was treated as a viscous (or no-slip boundary) surface. The grid used in this analysis consisted of 20 million nodes. Future analysis will consider a family of grids with a grid-convergence study. Topologically, the same surface density grid was inserted into the gridded representation of the TDT model, and the resulting volume grid size was about 80 million nodes. Figure 11b presents a picture of the KTH model inside the CFD model of the TDT. Although the experimental flutter event occurred with the under-the-wing stores and wing tip missiles attached, in this preliminary study and for simplicity, those were removed from the aerodynamic model. However, the finite element model (FEM) does include these parts in the form of point masses [15, 16]. The grid

topologies for the KTH-FA and the KTH-KTH models are presented in Figures 12a and 12b, respectively. The wind-tunnel grid topology assumed re-entry flaps at position #1. This contradicts the flap/Mach schedule presented in Figure 2, which dictates using the second flap setting at Mach 0.9. However, for that second flap position, the tunnel's cross-sectional area at the re-entry flap location increases by only about 1% over the corresponding area associated with re-entry flap position #1, and the size of the gap between the flaps and the ceiling and floor walls is less than an inch. Therefore, at Mach 0.9, it is a reasonable assumption to ignore flap re-entry position #2. However, future tunnel models will incorporate the correct re-entry flap position.

A dynamic flutter analysis process was employed using FUN3D software. The KTH dynamic analyses in free-air and in the TDT were performed in the same multistep process. First, the steady CFD solution was obtained on the rigid body. Results from this step, both the computed Mach numbers at the tunnel station 74 and the aircraft surface pressure distributions for the KTH-FA and KTH-TDT models, are presented in Figures 12c and 12d, respectively. Next, a static aeroelastic solution was obtained by restarting the CFD analysis from the rigid-steady solution in a time-accurate mode with a structural modal solver, allowing the grid to deform. A high value of structural damping (0.9999) and a fixed dynamic pressure were used so the structure could find its equilibrium position with respect to the mean flow before the dynamic response was started. For the KTH model in both free-air and in the TDT, the static aeroelastic surface deformation is very small and is not discussed here. Finally, the flutter solution was restarted from the static aeroelastic solution by setting the structural damping value to zero and providing an initial excitation 'kick' in the form of the generalized velocity. All of the flutter computations were run with a time-step size of 2×10^{-4} seconds [29]. Each KTH-FA flutter computation took approximately 5 days while the KTH-TDT simulation took 21 days on 1536 Sandy Bridge cores on the Pleiades computer at the NASA Advanced Supercomputing (NAS) Division and consists of an approximate 2-second long time history of the solution development.

For unsteady-flow analysis, the FUN3D solver utilizes the dual-time-stepping method, which is widely used in CFD [30]. This method involves adding a pseudo time derivative of the conserved variables to the physical time derivative that appears in the time-dependent Navier-Stokes equations. Aeroelastic analysis requires a grid deformation capability. The grid deformation in FUN3D is treated as a linear elasticity problem. In this approach, the grid points near the body can move significantly, while the points farther away may not move at all. In addition to the moving body capability, the analysis of the KTH configuration requires a structural dynamics capability. For a dynamic aeroelastic analysis, FUN3D is capable of being loosely coupled with an external finite element solver [31], or in the case of the linear structural dynamics used in this study, an internal modal structural solver can be utilized [32]. This modal solver is formulated and implemented in FUN3D in a manner similar to other NASA Langley aeroelastic codes (CAP-TSD [33] and CFL3D [34]). For the KTH computations presented here, the 25 structural modes were obtained via a normal modes analysis (solution 103) with the FEM solver MSC Nastran^{TM} [35]. The modes were then interpolated to the surface mesh using the method developed by Massey [36]. The z-displacements of four modes, modes 3, 4, 5, and 6, with modal frequencies of 8.0, 8.3, 11.7, and 12.0 Hz, respectively, in the vicinity of the experimental flutter frequency of 9.5 Hz are shown in Figure 13.

5.2 Results

The computed time histories of the generalized displacements for modes 3, 4, 5, and 6 for both the KTH-FA and KTH-TDT simulations are shown in Figure 14. Figures 14a, 14c, and

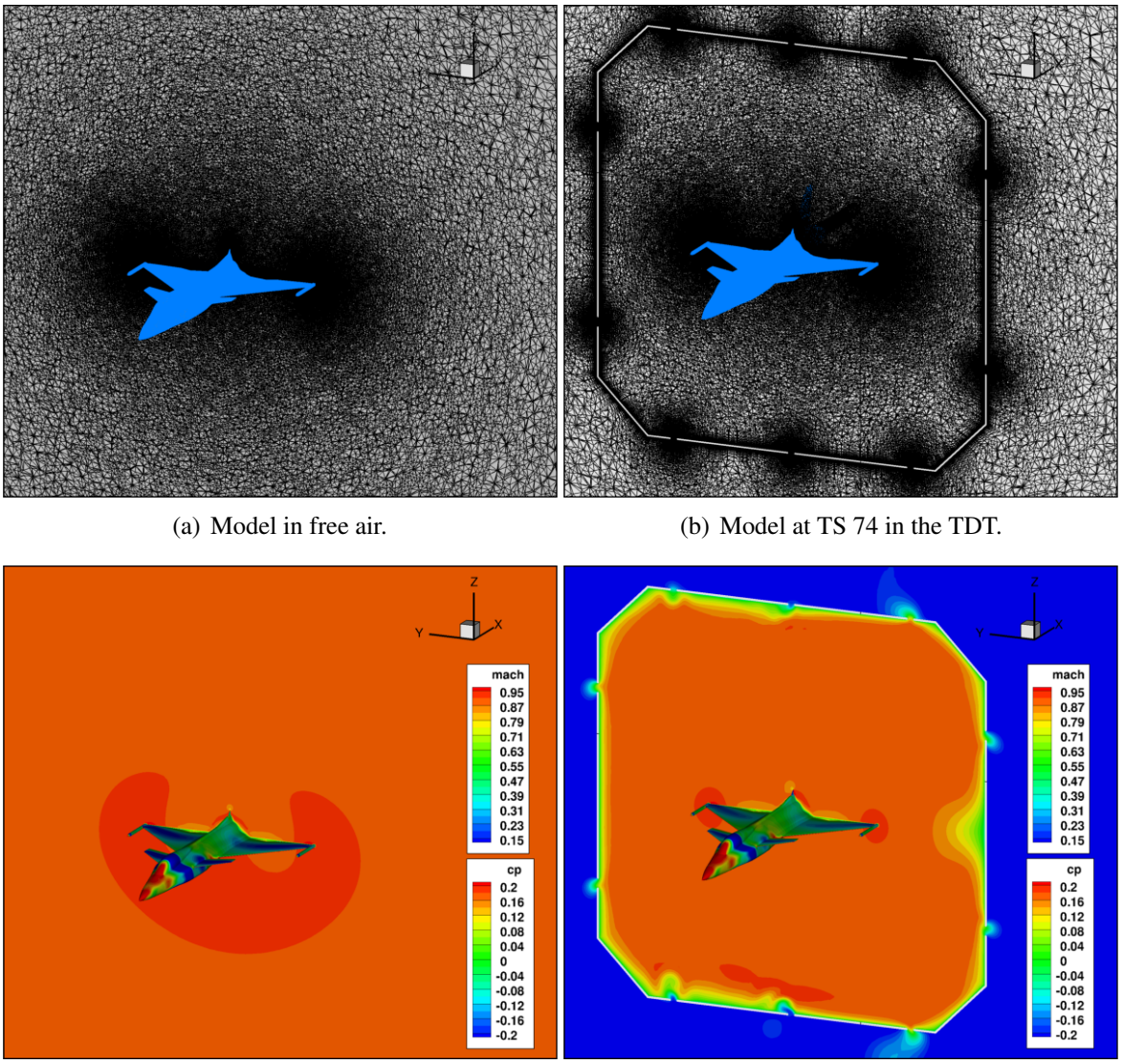

(a) Model in free air.

(b) Model at TS 74 in the TDT.

(c) Mach number and pressure contours in free air.

(d) Mach number and pressure contours at TS 74 in the TDT.

Figure 12: Grid topology and steady-state (rigid-body) solution for KTH-FA and the KTH-TDT models at Mach 0.9.

14e show results for the KTH-FA simulations at dynamic pressures of 3060, 7344, and 9180 Pa, respectively. Note, that since the finite element model is in the International System of Units (SI); therefore, unit of Pascal is used for the dynamic pressure. Corresponding results for the KTH-TDT simulations are provided in Figures 14b, 14d, and 14f. Several differences between the KTH-FA and KTH-TDT results need to be highlighted. First, the magnitude of the generalized displacement for the KTH-FA simulation is five times larger than the one for the KTH-TDT simulation. This amplitude difference is due to the initial excitation magnitude (generalized velocity) at the start of the dynamic simulation. An initial generalized velocity of '5' was used in the KTH-FA simulation, but this value was too large for the KTH-TDT simulation resulting in negative volumes. Consequently, a value of '1' was used for the KTH-TDT model simulation. Next, the system responses for all modes at Q of 9180 Pa for the KTH-FA simulation are gradually changing, with modes 3 and 5 unstable and modes 4 and 6 stable. This modal response is in contrast to the system response for the KTH-TDT simulation, where mode 5 is unstable, but it is difficult to establish stability for the other three modes.

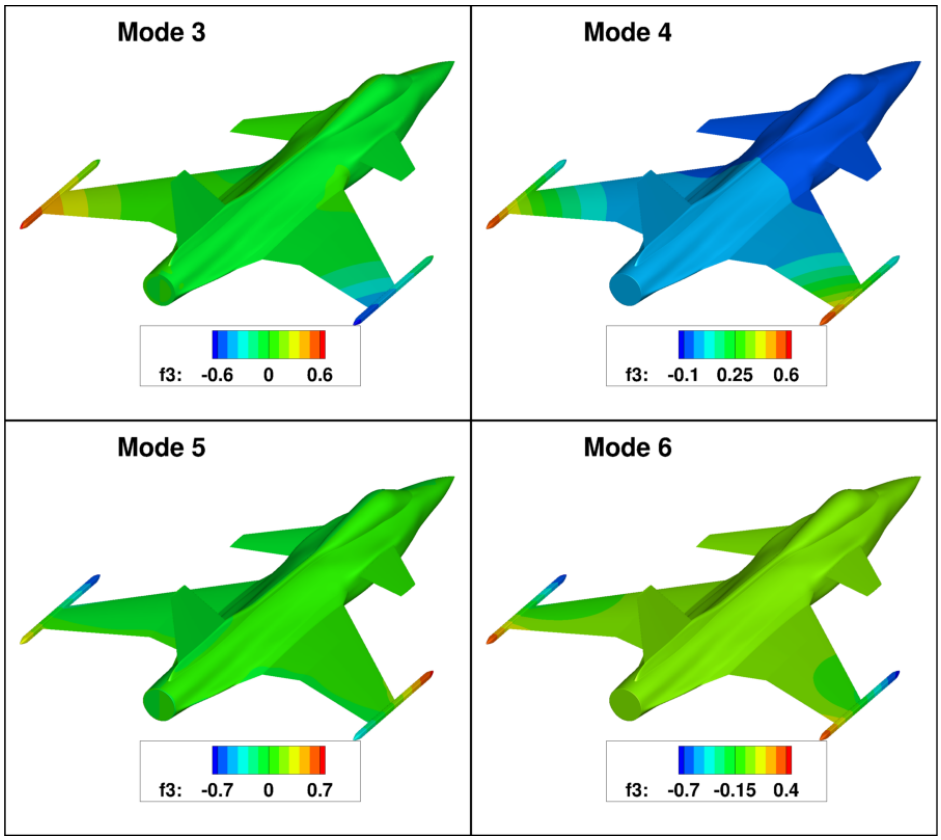

Figure 13: The z displacement, labeled as f3, of modes 3, 4, 5, and 6.

In addition, the mode 4 phase changes in time. At the dynamic pressure of 7344 Pa, both simulations show phase shift in modes 3 and 4. Both simulations also show stable responses at Q of 3060 Pa. Further analysis of the mode 5 response across all three dynamic pressures, indicates flutter dynamic pressures of 7745 Pa for the KTH-FA simulation and 7770 Pa for the KTH-TDT simulation. The flutter frequency was calculated to be 11 Hz for both simulations. By comparison, the experimental flutter dynamic pressure and frequency are close to 6600 Pa and 9.5 Hz, respectively.

There is a difference between how the flutter point is found experimentally and in the computations. In the experiment, the dynamic pressure and Mach number are varied as the flow conditions are traversed along a tunnel total pressure line. The goal is to slowly approach on a flutter point, transitioning to higher total pressure line until flutter is found or the model is cleared. Numerically in FUN3D, the total pressure and Mach number are held constant, while the dynamic pressure is varied on the structural solver side only without a feedback to the fluid side. Because of these differences, yet another step is required to bring numerical computations closer to the experiment. After the flutter point is found as described earlier, a 'match point condition' calculation is required. Here, based on the computed flutter dynamic pressure, the fluid properties need to be changed to match the dynamic pressure, and the entire solution process needs to be repeated. In this study, this step still needs to be completed.

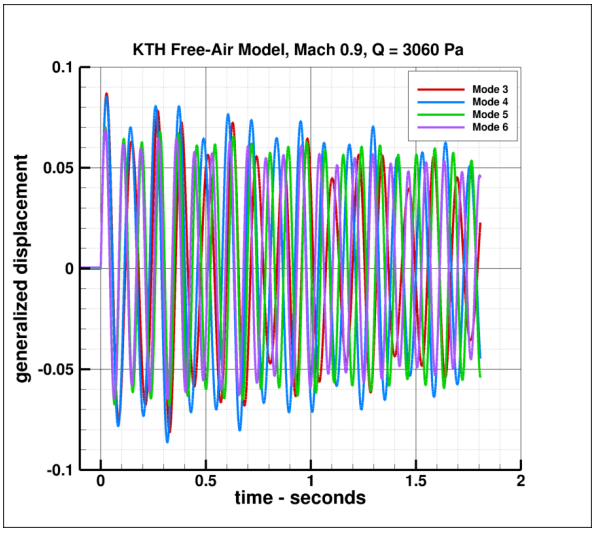

(a) KTH-FA, Q = 3060 Pa.

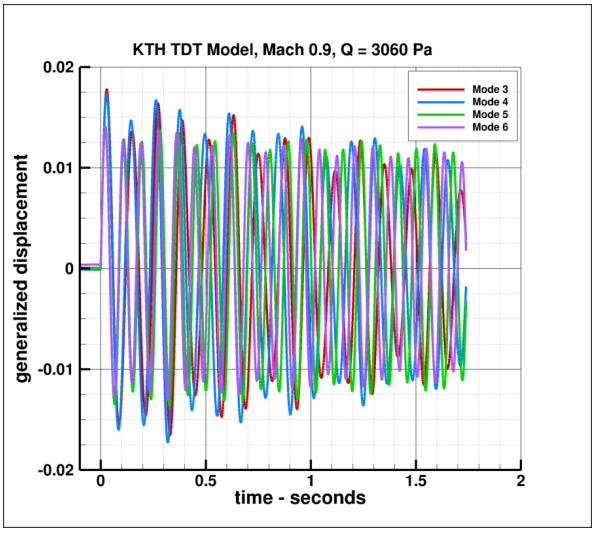

(b) KTH-TDT, Q = 3060 Pa.

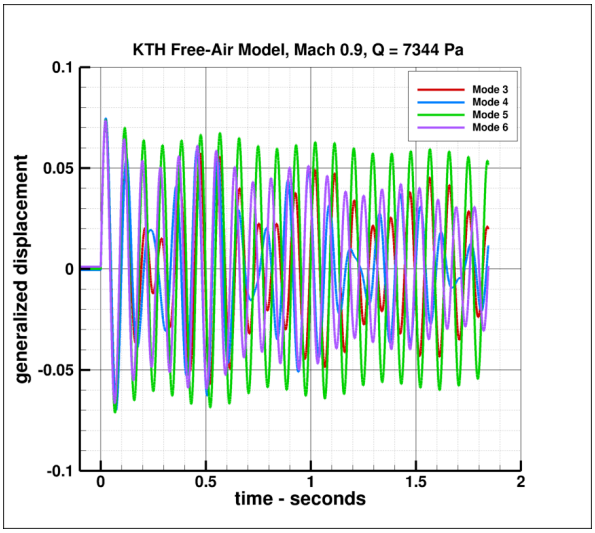

(c) KTH-FA, Q = 7344 Pa.

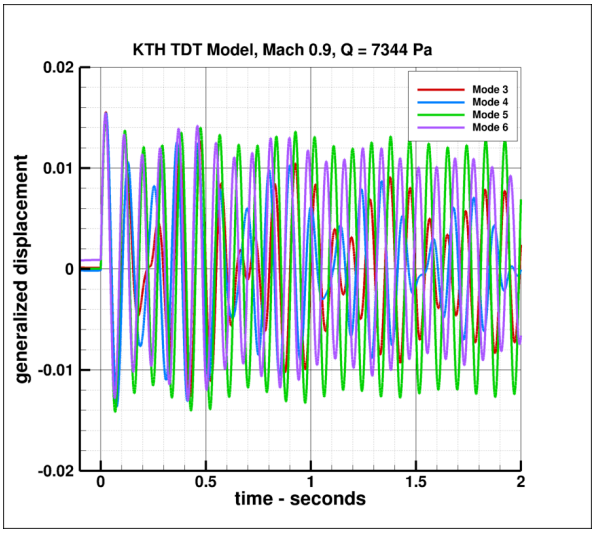

(d) KTH-TDT, Q = 7344 Pa.

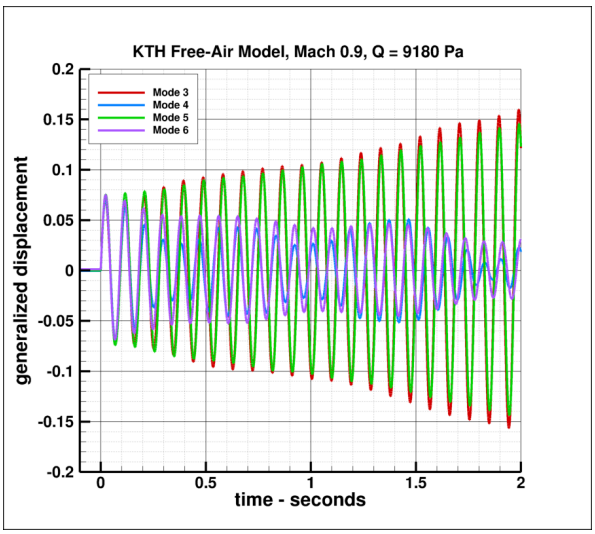

(e) KTH-FA, Q = 9180 Pa.

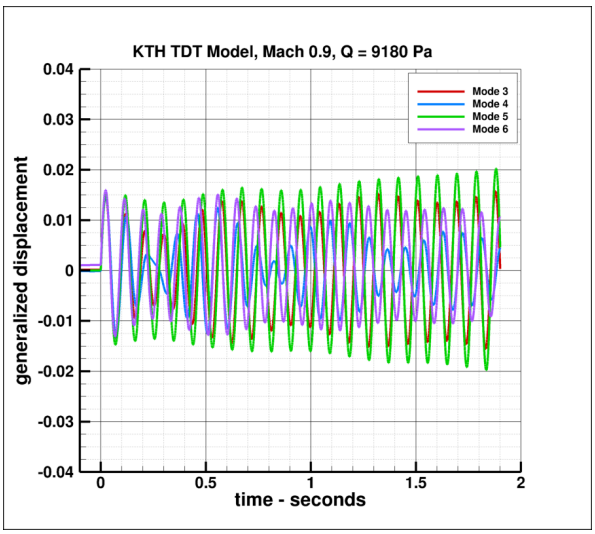

(f) KTH-TDT, Q = 9180 Pa.

Figure 14: Time history of the generalized displacements for KTH-FA and KTH-TDT simulations at three dynamic pressures Q: 3060, 7344, and 9180 Pa.

6 CONCLUDING REMARKS

The first objective of this study was to conduct CFD analysis of the empty TDT at Mach 0.5, 0.7, and 1.1 and then compare the computed wall pressures, boundary-layer profiles, and centerline Mach number distribution with the experimental data. The experimental and computational results compare well. However, additional work, both experimental and computational, is required to better understand the flow physics in a large tunnel like the TDT. A recommended list of potential future analysis and calibration experiments is as follows:

- In some instances, the actual shape of the slot edges changes from circular to wedge. However, the computational geometry used in this study assumed a circular shape of the slot edges throughout. A slot-edge- geometry modification will be incorporated in future analyses.
- The flow angle at the inlet boundary (normal to the inlet plane or a turning-vane angle) may have an influence on the boundary-layer profile downstream. A study to compute the flow angle influence needs to be completed.
- The location of the minimum cross-sectional area at tunnel station 44, based on the laser scan, was unexpected. This location was thought to be further downstream. A verification of this finding is necessary by reexamining the laser scan data. At the same time, further resolution of the mesh within the boundary layer is required to compute an effective aerodynamic cross-sectional area.
- It would be beneficial to measure the boundary layer upstream of the slots to obtain a data set that does not contain the flow-through-slots effects.
- Experimental back pressure measurements in the diffuser would eliminate the necessity of iterating on back pressure in the CFD analysis.

These are just a few examples and thoughts to consider. Future analyses will address the items listed above. In addition, analysis of the TDT with re-entry flap settings #2 and #3 at transonic Mach numbers will be conducted. Of course, the most important question is yet to be answered: Is it possible to model the entire circuit of the tunnel, including the geometric details of the turning vanes and motor drive, and capture boundary-layer profiles, wall pressures, and centerline Mach number distributions in the test section leg of the tunnel?

The second objective of this study was to compare flutter prediction for the KTH configuration assuming a free-air model and the model including the wind-tunnel walls. The preliminary assessment is that the wind-tunnel walls do affect the response of the aircraft, but the overall flutter prediction for both computational models is essentially the same. This finding is significant, since the excessive computational time needed to make these predictions makes it impractical to consider computational model which includes tunnel walls. Nevertheless, several items will be considered in the future analysis:

- The wing-tip missiles and the under-the-wing stores will be added to enhance the accuracy of the aerodynamic model.
- The finite element model (FEM) needs to be tuned based on the ground vibration test. Specifically, based on the ground vibration test, the frequency of the wing bending mode is lower than the corresponding FEM modal frequency.
- The grid resolution and temporal convergence study needs to be accomplished.
- The effect of the re-entry flap position on the flutter prediction will be addressed.
- The match-point calculation needs to be completed to verify the computed flutter dynamic pressure.

7 ACKNOWLEDGMENTS

This work is supported by the NASA Transformational Tools and Technologies and the Commercial Supersonics Technology projects. The computational analyses were conducted at the NAS Supercomputing Center at NASA Ames. The authors would like to acknowledge help from several members of the Aeroelasticity Branch at NASA Langley Research Center: Dr. Steve Massey, Dr. Bret Stanford, Mr. Don Keller, and Ms. Jennifer Pinkerton. In addition, the authors would like to acknowledge ongoing discussions with Professor Ulf Ringertz and David Eller of the Royal Institute of Technology in Sweden. Finally, CAD and some grid generation help from NASA's Geolab is greatly appreciated.

8 REFERENCES

[1] Ricketts, R. H., Sandford, M. C., Watson, J. J., et al. (1983). Geometric and Structural Properties of a Rectangular Supercritical Wing Oscillated in Pitch for Measurement of Unsteady Transonic Pressure Distributions. NASA TM 1983-85763.

[2] Ricketts, R. H., Sandford, M. C., Seidel, D. A., et al. (1983). Transonic Pressure Distributions on a Rectangular Supercritical Wing Oscillating in Pitch. NASA TM 1983-84616.

[3] Bennett, R. M. and Walker, C. E. (1999). Computational Test Cases for a Rectangular Supercritical Wing Undergoing Pitching Oscillations. NASA TM 1984-209130.

[4] Heeg, J., Chwalowski, P., Wieseman, C. D., et al. (2013). Lessons Learned in the Selection and Development of Test Cases for the Aeroelastic Prediction Workshop: Rectangular Supercritical Wing. AIAA Paper 2013-0784.

[5] Heeg, J., Chwalowski, P., Schuster, D. M., et al. (2013). Overview and Lessons Learned from the Aeroelastic Prediction Workshop. IFASD Paper 2013-1A.

[6] Heeg, J., Chwalowski, P., Schuster, D. M., et al. (2013). Overview and Lessons Learned from the Aeroelastic Prediction Workshop. AIAA Paper 2013-1798.

[7] Ivanco, T. G. (2013). Unique Testing Capabilities of the NASA Langley Transonic Dynamics Tunnel, an Exercise in Aeroelastic Scaling. AIAA Paper 2013-2625.

[8] Krynytzky, A. J. (2001). Steady-State Wall Interference of a Symmetric Half-Model in the Langley Transonic Dynamics Tunnel. AIAA Paper 2001-0161.

[9] Krynytzky, A. J. et al. (2010). Uncertainty Evaluation of Wall Interferences in a Large Transonic Wind Tunnel. AIAA Paper 2010-4341.

[10] Krynytzky, A. J. et al. (2012). Computational Modeling of a Slotted Wall Test Section. AIAA Paper 2012-2863.

[11] Glazkov, S. A. et al. (2004). Numerical and Experimental Investigations of Slot Flow with Respect to Wind Tunnel Interference Assessment. AIAA Paper 2004-2308.

[12] Olander, M. (2011). CFD Simulation of the Volvo Cars Slotted Walls Wind Tunnel. CHALMERS UNIVERSITY OF TECHNOLOGY, Göteborg, Sweden.

[13] Neumann, J. and Mai, H. (2013). Gust Response: Simulation of an Aeroelastic Experiment by a Fluid-Structure Interaction Method. *Journal of Fluids and Structures*. Vol. 38, April 2013, Pages 290-302.

[14] Massey, S. J., Kreshock, A. R., and Sekula, M. K. (2015). Coupled CFD/CSD Analysis of an Active-Twist Rotor in a Wind Tunnel with Experimental Validaton. AHS paper. American Helicopter Society 71st Annual Forum Proceedings.

[15] Silva, W. A., Ringertz, U., Stenfelt, G., et al. (2016). Status of the KTH-NASA Wind-Tunnel Test for Acquisition of Transonic Nonlinear Aeroelastic Data. AIAA Paper 2016-2050.

[16] Silva, W. A., Chwalowski, P., Wieseman, C. D., et al. (2017). Computational Results for the KTH-NASA Wind-Tunnel Model Used for Acquisition of Transonic Nonlinear Aeroelastic Data. AIAA Paper 2017-1814.

[17] Silva, W. A., Chwalowski, P., Wieseman, C. D., et al. Computational and Experimental Results for the KTH-NASA Wind-Tunnel Model Used for Acquisition of Transonic Nonlinear Aeroelastic Data. IFASD Paper 2017-181.

[18] Nayani, S. N., Sellers, W. L., Brynildsen, S. E., et al. (2015). Numerical Study of the High-Speed Leg of a Wind Tunnel. AIAA Paper 2015-2022.

[19] Chwalowski, P., Quon, E., and Brynildsen, S. E. (2016). Computational Analysis of the Transonic Dynamics Tunnel. AIAA Paper 2016-1775.

[20] Pirzadeh, S. Z. Advanced Unstructured Grid Generation for Complex Aerodynamic Applications. AIAA Paper 2008-7178.

[21] Samareh, J. A. Unstructured Grids on NURBS Surfaces. AIAA Paper 1993-3454.

[22] NASA LaRC, Hampton, VA (2015). *FUN3D Manual, v12.9*. http://fun3d.larc.nasa.gov.

[23] Roe, P. L. Characteristic-Based Schemes for the Euler Equations. *Ann. Rev. Fluid Mech.* Vol. 18, Pages 337-365.

[24] Roe, P. L. Approximate Riemann Solvers, Parameter Vectors, and Difference Schemes. *Journal of Computational Physics*. Vol. 43, No. 2, 1981.

[25] Wieseman, C. D. and Bennett, R. M. (2007). Wall Boundary Layer Measurements for the NASA Langley Transonic Dynamics Tunnel. NASA TM 2007-214867.

[26] Tecplot, Bellevue, WA 98015 (2013). *Tecplot*. http://www.tecplot.com/products/tecplot-360/.

[27] Florance, J. R. and Rivera, J. A. (2001). Sidewall Mach Number Distributions for the NASA Langley Transonic Dynamics Tunnel. NASA TM 2001-211019.

[28] Keller, D. (2013). Private communication, NASA Langley Research Center, Hampton, VA.

[29] Chwalowski, P., Heeg, J., and Biedron, R. T. (2017). Numerical Investigations of the Benchmark Supercritical Wing in Transonic Flow. AIAA Paper 2017-0190.

[30] Biedron, R. T., Vatsa, V. N., and Atkins, H. L. (2005). Simulation of Unsteady Flows Using an Unstructured Navier-Stokes Solver on Moving and Stationary Grids. AIAA Paper 2005-5093.

[31] Biedron, R. T. and Lee-Rausch, E. M. Rotor Airloads Prediction Using Unstructured Meshes and Loose CFD/CSD Coupling. AIAA Paper 2008-7341.

[32] Biedron, R. T. and Thomas, J. L. (2009). Recent Enhancements to the FUN3D Flow Solver for Moving-Mesh Applications. AIAA Paper 2009-1360.

[33] Batina, J. T., Seidel, D. A., Bland, S. R., et al. Unsteady Transonic Flow Calculations for Realistic Aircraft Configurations. AIAA Paper 1987-0850.

[34] Bartels, R. E., Rumsey, C. L., and Biedron, R. T. CFL3D Version 6.4 - General Usage and Aeroelastic Analysis. NASA TM 2006-214301 March 2006.

[35] MSC Software, Santa Ana, CA (2008). *MSC Nastran*. http://www.mscsoftware.com/.

[36] Massey, S. (2017). Radial Basis Function Method, Private communication, NASA Langley Research Center, Hampton, VA.

9 COPYRIGHT STATEMENT